
Decoupled Diffusion Models with Explicit Transition Probability

Yuhang Huang

National University of Defense Technology
huangai@nudt.edu.cn

Zheng Qin

National University of Defense Technology
qinzheng12@nudt.edu.cn

Xinwang Liu

National University of Defense Technology
xinwangliu@nudt.edu.cn

Kai Xu

National University of Defense Technology
kevin.kai.xu@gmail.com

Abstract

Recent diffusion probabilistic models (DPMs) have shown remarkable abilities of generated content, however, they often suffer from complex forward processes, resulting in inefficient solutions for the reversed process and prolonged sampling times. In this paper, we aim to address the aforementioned challenges by focusing on the diffusion process itself that we propose to decouple the intricate diffusion process into two comparatively simpler process to improve the generative efficacy and speed. In particular, we present a novel diffusion paradigm named DDM (**Decoupled Diffusion Models**) based on the Itô diffusion process, in which the image distribution is approximated by an explicit transition probability while the noise path is controlled by the standard Wiener process. We find that decoupling the diffusion process reduces the learning difficulty and the explicit transition probability improves the generative speed significantly. We prove a new training objective for DPM, which enables the model to learn to predict the noise and image components separately. Moreover, given the novel forward diffusion equation, we derive the reverse denoising formula of DDM that naturally supports fewer steps of generation without ordinary differential equation (ODE) based accelerators. Our experiments demonstrate that DDM outperforms previous DPMs by a large margin in fewer function evaluations setting and gets comparable performances in long function evaluations setting. We also show that our framework can be applied to image-conditioned generation and high-resolution image synthesis, and that it can generate high-quality images with only 10 function evaluations.

1 Introduction

Recent diffusion probabilistic models (DPMs) [13, 27, 12, 6] have shown state-of-the-art performances in generated content fields such as image and speech synthesis [16, 3, 4], image-to-image translation [31], and 3D object generation [23, 28]. Different from variational auto-encoders [18] or adversarial models [11], DPMs view the image-to-noise process as a parameterized Markov chain that gradually adds noise to the original data until the signal is completely corrupted, and utilize a neural network to model the *reversed denoising process* for new samples generation.

Song et al. [36] have proved that the *forward diffusion process* of DPMs is equivalent to the score-based generative models (SGMs) [32, 35, 17] that can be represented by a stochastic differential equation (SDE). Essentially, the training objective of DPMs is to learn the score function—the gradient of the log probability density—of the perturbed data, and synthesizing new samples aims to solve the reverse-time SDE using the learned score function. Moreover, Song et al. show that the learned score function is uniquely dependent on the forward diffusion process. Therefore, the complexity of training DPMs depends largely on the forward diffusion formulation, which means that

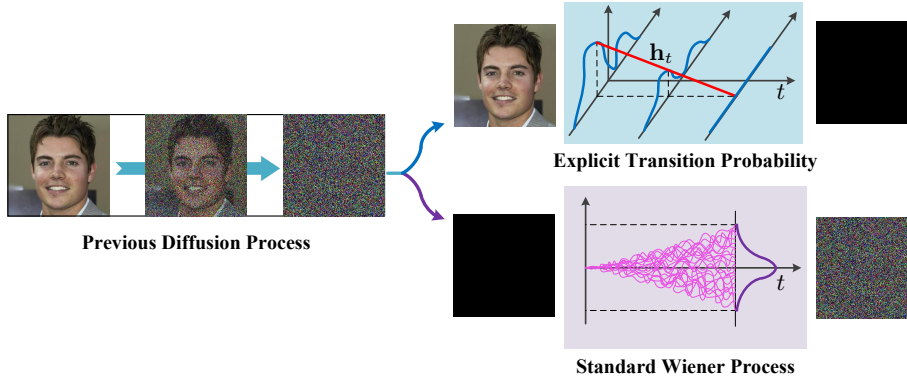


Figure 1: Overview framework. Different from previous diffusion process, we propose to split the complex mapping from the image to noise into two relatively simpler processes: the annihilation of image component and the increasing of noise component. We use an explicit transition probability to approximate the attenuation gradient of the image (we draw the uniform attenuation gradient in the red curve as an example). Meanwhile, the noise path is governed by the standard Wiener process, enabling the zero image to progressively increase to the standard normal noise.

the most critical step to enhance the generation capability of DPMs is to create a versatile diffusion process.

Current DPMs or SGMs usually construct the forward diffusion process as a typically complex SDE that meticulously manages the amount of image and noise changes at each time step, converting the modeling of the score function into a predictive noise component. However, the complexity of the SDE hampers the generative capabilities of DPMs. On the one hand, the corrupted signals at intermediate times of the diffusion process are strongly coupled with both the original data and the noise, making it difficult to distinguish the noise component. As a result, predicting the noise component from the corrupted signals is arduous. On the other hand, since the corresponding reverse-time SDE inherits the complexity of the forward one, solving it accurately requires numerical integration with very small step sizes, resulting in thousands of function evaluations [36]. We empirically reveal a deep coupling between the image and noise components in the diffusion process, making it difficult to solve the reverse SDE accurately. Hence, we contemplate the possibility of decoupling the diffusion process into relatively simpler processes, enabling more precise and efficient solutions to the reversed process.

Following this idea, we propose a new diffusion paradigm, Decoupled Diffusion Models (DDM), to decouple the image and noise components from the diffusion process. As shown in Fig. 1, previous diffusion processes directly build a complex mapping from the clean image to noise, which ignores the coupling of the noise and image. To decouple these two components, we propose to split the complex mapping into two relatively simpler parts: the annihilation process of the original data and the increase process of the noise. Through decoupling the complex process, we can model the two simpler processes independently and design the two pathways in a more flexible way. We theoretically prove that the decoupled diffusion process is equivalent to the original forward diffusion process based on the fact they both describe the same mapping from image to noise. Furthermore, we formulate the training objective for this innovative process, highlighting the independent learning of the noise and image components by the model. Moreover, we derive the formula for solving the reverse-time process, illustrating that DDM can sample using any step size.

Specifically, we introduce a novel SDE based on the Itô process [20] to decouple the image and the noise components, in which the drift term makes the image component decrease gradually while the diffusion term controls the increase of noise. On the one hand, by breaking down the complex mapping from the original data to noise into two relatively simpler processes, we can reduce the learning difficulty of the model as indicated in our toy examples (as shown in Fig. 2). On the other hand, it is difficult to derive an analytical solution for the typically complex reverse-time SDE, which limits the step size of numerical integration. Therefore, we propose to model the distribution of image components using an explicit transition probability that matches the opposite direction of the gradient of the image over time. Since the explicit transition probability makes it possible to seek an approximative analytical solution of the image component, we can quickly solve the reversed-time

SDE with an arbitrary step size, reducing the number of function evaluations significantly. Leveraging the explicit transition probability and the decoupled SDE, DDM demonstrates the capability to generate high-quality content while minimizing the number of function evaluations required.

In summary, we present a novel diffusion model theoretically and demonstrate its superiority to previous DPMs experimentally. Our contributions can be divided into three-fold:

- A novel diffusion paradigm named DDM, which decouples the noise component and the image component from the diffusion process.
- A novel forward diffusion SDE and its training objective that enables the model to learn the image and noise components respectively. Additionally, we derive the reverse denoising formula of DDM that naturally supports fewer steps of generation.
- Extensive experiments on various tasks including unconditional and conditional generation demonstrate the significant advantages.

2 Background

The forward diffusion process of a typical DPM [32] is described as a Markov chain. Consider a continuous-time Markov chain with $t \in [0, 1]$:

$$q(\mathbf{x}_t|\mathbf{x}_0) = \mathcal{N}(\mathbf{x}_t; \alpha_t\mathbf{x}_0, \beta_t^2\mathbf{I}), \quad (1)$$

where α_t, β_t are differentiable functions of time t with bounded derivatives. β_t is designed to increase gradually over time while α_t does the opposite, ensuring $q(\mathbf{x}_1|\mathbf{x}_0) = \mathcal{N}(\mathbf{x}_1; \mathbf{0}, \mathbf{I})$. It has been proven that the aforementioned Markov chain can be represented by the following SDE [17]:

$$d\mathbf{x}_t = f_t\mathbf{x}_tdt + g_td\mathbf{w}_t, \quad \mathbf{x}_0 \sim q(\mathbf{x}_0), \quad (2)$$

where $f_t = \frac{d \log \alpha_t}{dt}$, $g_t^2 = \frac{d\beta_t^2}{dt} - 2f_t\beta_t^2$, and \mathbf{w}_t is the standard Wiener process. Song et al. [36] show that the corresponding reversed SDE inverting \mathbf{x}_1 to \mathbf{x}_0 can be derived:

$$d\mathbf{x}_t = [f_t\mathbf{x}_t - g_t^2\nabla_{\mathbf{x}} \log q(\mathbf{x}_t)]dt + g_td\bar{\mathbf{w}}_t, \quad (3)$$

where $\bar{\mathbf{w}}_t$ is a standard Wiener process in the reverse-time. To this end, the only unknown term in Eq. 3 is $\nabla_{\mathbf{x}} \log q(\mathbf{x}_t)$, which is parameterized by a neural network $\epsilon_{\theta}(\mathbf{x}_t, t)$ with the parameters θ . $\epsilon_{\theta}(\mathbf{x}_t, t)$ estimates the scaled score function, i.e., $-\beta_t\nabla_{\mathbf{x}} \log q(\mathbf{x}_t)$, and the training objective [13] is:

$$\begin{aligned} \mathcal{L}(\theta, \lambda_t) &:= \int_0^1 \lambda_t \mathbb{E}_{q(\mathbf{x}_0)} \mathbb{E}_{q(\epsilon)} [\|\epsilon_{\theta}(\mathbf{x}_t, t) + \beta_t \nabla_{\mathbf{x}} \log q(\mathbf{x}_t)\|^2] dt \\ &= \int_0^1 \lambda_t \mathbb{E}_{q(\mathbf{x}_0)} \mathbb{E}_{q(\epsilon)} [\|\epsilon_{\theta}(\mathbf{x}_t, t) - \epsilon\|^2] dt, \end{aligned} \quad (4)$$

where $\epsilon \sim \mathcal{N}(\epsilon; \mathbf{0}, \mathbf{I})$, $\mathbf{x}_t = \alpha_t\mathbf{x}_0 + \beta_t\epsilon$, and λ_t is a weighting function.

Replacing the score function by $\epsilon_{\theta}(\mathbf{x}_t, t)$ in Eq. 3, one can generate samples by solving the following reversed SDE with numerical integration, starting from $\mathbf{x}_1 \sim \mathcal{N}(\mathbf{x}_1; \mathbf{0}, \mathbf{I})$:

$$d\mathbf{x}_t = [f_t\mathbf{x}_t + \frac{g_t^2}{\beta_t}\epsilon_{\theta}(\mathbf{x}_t, t)]dt + g_td\bar{\mathbf{w}}_t. \quad (5)$$

However, due to the complexity of the SDE, it is difficult to estimate the score function accurately and to find an analytical solution for the reverse-time SDE. As a result, DPMs need thousands of function evaluations to generate high-quality images, resulting in extremely long inference time.

3 Method

In this section, we present DDM, a new diffusion paradigm which decouples the image and noise components from the diffusion process. Unlike previous pipelines, the forward SDE of DDM comprises two independent terms: a drift term gradually degrades the original image to zero, and a diffusion term transforms the zero image to standard normal noise along the time.

In the following, we first analyze the efficacy of each step in the reversed denoising process and reveal the effectiveness of decoupling the complex SDE into two simpler processes. Based on this

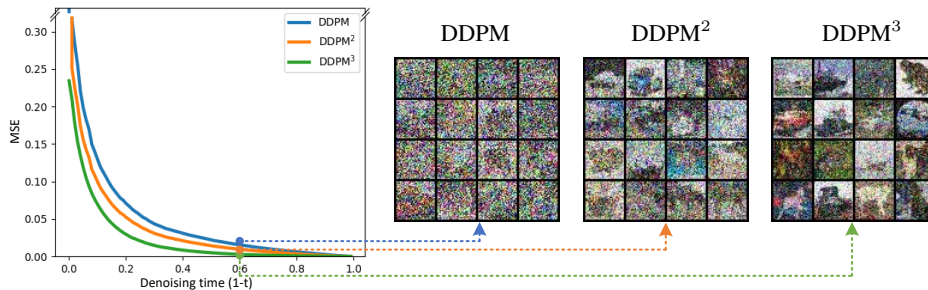


Figure 2: Toy examples. We evaluate the efficacy of each step using the MSE of the final \mathbf{x}_0 and the estimated $\hat{\mathbf{x}}_0$ during denoising time. As shown in the figure, DDPM² predicts the noise and image components simultaneously, getting a better performance than DDPM, while DDPM³ decouples the two parts more thoroughly, obtaining the best efficacy and visual result.

insight, we propose a new forward diffusion SDE that decouples the complex transformation from image to noise. We derive the training objective specific to DDM and demonstrate that our model learns the noise and image components separately. Furthermore, we derive the sampling formula utilized in the reverse-time process and show that DDM can generate new samples more efficiently.

3.1 Toy Examples

To explore how to improve the effectiveness of DPMs, we construct a series of variants to compare the efficacy of each reversed step. As we can get an approximate estimation of \mathbf{x}_0 by the forward transition probability $q(\mathbf{x}_t|\mathbf{x}_0)$ for any time t in the reverse-time process, we use the mean squared error (MSE) between the estimated $\hat{\mathbf{x}}_0$ and \mathbf{x}_0 to evaluate the efficacy of time t .

Here we take DDPM [13] with a small U-net architecture (48M parameters) as our baseline and only use the noise loss [13] to train the network. Since DDPM utilizes the discrete time from 1 to 1000, we align it with the continuous time $t \in [0, 1]$ that each step is equivalent to 0.001. As shown in Fig. 2, the baseline fails to get a prediction close to \mathbf{x}_0 until $t \approx 0.1$, indicating its inefficiency. We assume that the noise component is highly coupled to the original image in \mathbf{x}_t , making prediction extremely difficult. To this end, we introduce an additional branch to predict \mathbf{x}_0 . This model is named DDPM². With this simple modification, DDPM² reaches the converged result at an earlier time $t \approx 0.2$, demonstrating the usefulness of predicting noise and image components separately. To delve deeper into this, we further decouple the mapping from image to noise into two simpler parts: a image-to-zero process and a zero-to-noise process. For a simple test, we consider the image-to-zero process to be linearly descending and the variance of zero-to-noise to be linearly increasing. Consequently, the forward transition probability of DDPM is rewritten as:

$$q(\mathbf{x}_t|\mathbf{x}_0) = \mathcal{N}(\mathbf{x}_t; (1-t)\mathbf{x}_0, t\mathbf{I}). \quad (6)$$

We refer to this method as DDPM³ and supervise the U-net using the \mathbf{x}_0 and noise simultaneously. As a result, DDPM³ shows the best efficacy and converges at the earliest time $t \approx 0.4$.

3.2 Decoupled Diffusion Models with Explicit Transition Probability

The preliminary experiments provide guidance for improving the generative abilities of DPMs, however, it cannot handle the numerical integration that require thousands of function evaluations when solving the reverse-time SDE. From another perspective, the curves in Fig. 2 can be viewed as the variation of \mathbf{x}_t with respect to t ; that is, if we obtain the explicit expression of $\frac{d\mathbf{x}_t}{dt}$, the reversed process can be expedited by the analytical solution. Building on this insight, our DDM models the gradient of the image component as an explicit and differentiable function, offering the advantages of high efficacy and high speed.

We introduce a forward process and a reversed process, representing the pathways of image corruption and denoising, respectively. Then, we prove that the proposed forward decoupled process is equivalent to previous mapping from image to noise based on the fact they describe the same mapping from image to noise. To demonstrate its effectiveness, we derive the novel training objective by maximizing the evidence lower bound of the log-likelihood. Finally, we utilize the Bayesian theorem to derive the sampling formula of DDM which naturally enables few-step generations.

Forward Process. Specifically, we propose a novel diffusion formula based on Itô process to describe the forward process:

$$\mathbf{x}_t = \mathbf{x}_0 + \int_0^t \mathbf{h}_t dt + \int_0^t d\mathbf{w}_t, \quad \mathbf{x}_0 \sim q(\mathbf{x}_0). \quad (7)$$

Here, $\mathbf{x}_0 + \int_0^t \mathbf{h}_t dt$ corresponds to the attenuation process of the image, while $\int_0^t d\mathbf{w}_t$ controls the increasing noise, \mathbf{w}_t is the standard Wiener process and \mathbf{h}_t is a differentiable function of t . We prove that the proposed decoupled diffusion process is equivalent to the previous SDE in *supplementary material*. The forward process must ensure that $\mathbf{x}_t \sim q(\mathbf{x}_0)$ when $t = 0$ and $\mathbf{x}_t \sim \mathcal{N}(\mathbf{x}_1; \mathbf{0}, \mathbf{I})$ when $t = 1$. Obviously, the latter term satisfies the requirements cause $\int_0^t d\mathbf{w}_t = \mathbf{w}_t - \mathbf{w}_0 \sim \mathcal{N}(\mathbf{0}, t\mathbf{I})$. Therefore, it is only necessary to design an explicit function \mathbf{h}_t that satisfies: $\mathbf{x}_0 + \int_0^1 \mathbf{h}_t dt = \mathbf{0}$. Eq. 7 shows that $q(\mathbf{x}_t|\mathbf{x}_0)$ can be regarded as a normal distribution with mean $\mathbf{x}_0 + \int_0^t \mathbf{h}_t dt$ and variance $t\mathbf{I}$. For simplicity, we denote $\mathbf{H}_t = \int_0^t \mathbf{h}_t dt$ and give the forward transition probability similar to Eq. 6:

$$q(\mathbf{x}_t|\mathbf{x}_0) = \mathcal{N}(\mathbf{x}_t; \mathbf{x}_0 + \mathbf{H}_t, t\mathbf{I}). \quad (8)$$

Thus, we can sample \mathbf{x}_t by $\mathbf{x}_t = \mathbf{x}_0 + \mathbf{H}_t + \sqrt{t}\epsilon$ in the forward process, where $\epsilon \sim \mathcal{N}(\mathbf{0}, \mathbf{I})$.

Reversed Process. Based on the forward transition probability, we can build the reversed transition probability through the Bayesian theorem. Unlike DDPM [13] which utilizes the discrete-time transition probability, we employ the continuous-time transition probability with the smallest time step $\Delta t \rightarrow 0^+$ and use the conditional distribution $q(\mathbf{x}_{t-\Delta t}|\mathbf{x}_t, \mathbf{x}_0)$ to approximate $q(\mathbf{x}_{t-\Delta t}|\mathbf{x}_t)$:

$$q(\mathbf{x}_{t-\Delta t}|\mathbf{x}_t, \mathbf{x}_0) = \frac{q(\mathbf{x}_t|\mathbf{x}_{t-\Delta t}, \mathbf{x}_0)q(\mathbf{x}_{t-\Delta t}|\mathbf{x}_0)}{q(\mathbf{x}_t|\mathbf{x}_0)}. \quad (9)$$

Given the forward diffusion formula, we can derive that the reversed transition probability $q(\mathbf{x}_{t-\Delta t}|\mathbf{x}_t, \mathbf{x}_0)$ is also a normal distribution:

$$\begin{aligned} q(\mathbf{x}_{t-\Delta t}|\mathbf{x}_t, \mathbf{x}_0) &\propto \exp\left\{-\frac{(\mathbf{x}_{t-\Delta t} - \tilde{\mathbf{u}})^2}{2\tilde{\sigma}^2\mathbf{I}}\right\}, \\ \tilde{\mathbf{u}} &= \mathbf{x}_t + \mathbf{H}_{t-\Delta t} - \mathbf{H}_t - \frac{\Delta t}{\sqrt{t}}\epsilon, \\ \tilde{\sigma}^2 &= \frac{\Delta t(t - \Delta t)}{t}, \end{aligned} \quad (10)$$

where $\epsilon \sim \mathcal{N}(\mathbf{0}, \mathbf{I})$. The non-parametric variance term is solely dependent on the current time t and the step size Δt , whereas the mean term involves two unknown variables: \mathbf{H}_t and ϵ . As a result, to solve the reversed process, we must parameterize \mathbf{H}_t and ϵ using a neural network. Please refer to the supplementary material for more details.

3.3 Training Objective

Essentially, the value of \mathbf{H}_t depends on \mathbf{h}_t which is an explicit function with respect to t . In turn, \mathbf{h}_t is determined by its hyper-parameters ϕ , that can be solved using $\mathbf{x}_0 + \int_0^1 \mathbf{h}_t dt = \mathbf{0}$. In practice, we parameterize ϕ and ϵ by the U-net architecture with two decoder branches, such that they are obtained as the outputs of the network: $\phi_\theta, \epsilon_\theta = \text{Net}_\theta(\mathbf{x}_t, t)$.

By maximizing the evidence lower bound of the log-likelihood $\log p(\mathbf{x})$, we demonstrate the training objective of DDM (please refer to the supplementary material for further details):

$$\min_{\theta} \mathbb{E}_{q(\mathbf{x}_0)} \mathbb{E}_{q(\epsilon)} [\|\phi_\theta - \phi\|^2 + \|\epsilon_\theta - \epsilon\|^2]. \quad (11)$$

The initial term in the training objective corresponds to the image component, while the subsequent term corresponds to the noise component. This implies that the model is trained to learn the image and noise independently, in line with our objective of decoupling the clean image and noise components from \mathbf{x}_t . From an abstract viewpoint, the noise represents the starting point in the reverse-time process for \mathbf{x}_t , whereas the clean image represents the endpoint. Simultaneously predicting the image and noise components enables \mathbf{x}_t to be aligned with both starting and ending points at each time step. The detailed training procedure is presented in Alg. 1.

Algorithm 1 Training algorithm of DDM.

```
1: Initialize  $i = 0, N = num\_iters, lr, Net_{\theta}$ ;  
2: while  $i < N$  do  
3:    $t \sim Uniform(0, 1), \mathbf{x}_0 \sim q(\mathbf{x}_0), \boldsymbol{\epsilon} \sim \mathcal{N}(\mathbf{0}, \mathbf{I}), \phi \sim \mathbf{x}_0 + \mathbf{H}_1 = \mathbf{0}$ ;  
4:    $\mathbf{H}_t = \int_0^t \mathbf{h}_t^{\phi} dt$ ;  
5:    $\mathbf{x}_t = \mathbf{x}_0 + \mathbf{H}_t + \sqrt{t}\boldsymbol{\epsilon}$ ;  
6:    $\phi_{\theta}, \boldsymbol{\epsilon}_{\theta} = Net_{\theta}(\mathbf{x}_t, t)$ ;  
7:    $\boldsymbol{\theta} \leftarrow lr * \nabla_{\boldsymbol{\theta}}(\|\phi_{\theta} - \phi\|^2 + \|\boldsymbol{\epsilon}_{\theta} - \boldsymbol{\epsilon}\|^2)$ ;  
8:    $i = i + 1$ ;  
9: end while;  
10: return  $Net_{\theta}$ ;
```

3.4 Few-step Sampling from DDM

We have detailed the reverse-time process in the preceding section. Therefore, we can directly sample from DDM by iteratively solving Eq. 10 from $t = 1$ to 0. As \mathbf{h}_t is explicit, DDM possesses the natural property of sampling with an arbitrary step size s . Consequently, we can derive the expression for $q(\mathbf{x}_{t-s}|\mathbf{x}_t, \mathbf{x}_0)$ as proved in supplementary material:

$$\begin{aligned} q(\mathbf{x}_{t-s}|\mathbf{x}_t, \mathbf{x}_0) &\propto \exp\left\{-\frac{(\mathbf{x}_{t-s} - \tilde{\mathbf{u}})^2}{2\tilde{\sigma}^2\mathbf{I}}\right\}, \\ \tilde{\mathbf{u}} &= \mathbf{x}_t + \mathbf{H}_{t-s} - \mathbf{H}_t - \frac{s}{\sqrt{t}}\boldsymbol{\epsilon}, \\ \tilde{\sigma}^2 &= \frac{s(t-s)}{t}. \end{aligned} \tag{12}$$

The sampling equation suggests that we can even generate images in a single step. Nevertheless, it is challenging to estimate an exactly accurate ϕ at the initial time, and one-step generation causes the variance $\tilde{\sigma}^2$ to be zero. This results in the generated images appearing somewhat blurry and lacking diversity. Therefore, we still sample iteratively but use a much larger step size than previous DPMs, reducing the sampling steps from 1000 to 10 drastically. We commence at $t = 1$ and take uniform steps of size s until we reach $t = 0$. The algorithmic details are outlined in Alg. 2.

Algorithm 2 Sampling algorithm of DDM.

```
1: Initialize  $\mathbf{O} \sim \mathcal{N}(\mathbf{0}, \mathbf{I}), t = 1, N = num\_steps, s = 1/N, Net_{\theta}$ ;  
2: while  $t > 0$  do  
3:    $\phi_{\theta}, \boldsymbol{\epsilon}_{\theta} = Net_{\theta}(\mathbf{x}_t, t)$ ;  
4:    $\mathbf{H}_t = \int_0^t \mathbf{h}_t^{\phi} dt$ ;  
5:    $\tilde{\mathbf{u}} = \mathbf{O} + \mathbf{H}_{t-s} - \mathbf{H}_t - \frac{s}{\sqrt{t}}\boldsymbol{\epsilon}_{\theta}$ ;  
6:    $\tilde{\sigma} = \sqrt{\frac{s(t-s)}{t}}$ ;  
7:    $\mathbf{O} = \tilde{\mathbf{u}} + \tilde{\sigma} * \tilde{\boldsymbol{\epsilon}}, \tilde{\boldsymbol{\epsilon}} \sim \mathcal{N}(\mathbf{0}, \mathbf{I})$ ;  
8:    $t = t - s$ ;  
9: end while;  
10: return  $\mathbf{O}$ ;
```

4 Experiments

4.1 Experimental Setup

Implementation Details. We perform main experiments on unconditional image generation and conduct conditional image generation tasks to demonstrate the generalizability of our approach in various scenarios. For unconditional image generation, we evaluate DDM on the low-resolution CIFAR-10 dataset [19], as well as on high-resolution datasets CelebA-HQ-256 [15]. For conditional image generation, we conduct three sub-tasks: image inpainting on CelebA-HQ-256, super resolution on DIV2K [1], and semantic map to image on Cityscapes [5]. Due to the limitations of compute resources, we translate the diffusion process into latent space for high-resolution image synthesis

Table 1: Unconditional generative performances (FID \downarrow) on CIFAR-10 and CelebA-HQ-256 compared to previous DPMs. We do not run the 2000-step sampling on CelebA-HQ-256, because it takes too much time for one test (more than 7 days on a RTX 3090 GPU).

Dataset	Method \NFE	10	20	50	1000	2000
CIFAR-10	DDPM [13]	296.84	140.68	38.36	3.17	-
	SDE [36]	425.67	250.29	101.43	2.39	2.20
	LSGM [38]	27.64	11.69	5.19	2.19	-
	CLD [7]	415.36	162.44	52.70	2.27	2.23
	Ours	13.92	8.99	5.09	2.40	2.19
CelebA-HQ-256	SDE [36]	430.84	210.54	78.98	7.25	-
	LSGM [38]	27.53	14.39	13.85	7.23	-
	CLD [7]	355.15	179.85	64.77	8.06	-
	Ours	27.45	14.37	11.72	7.10	-

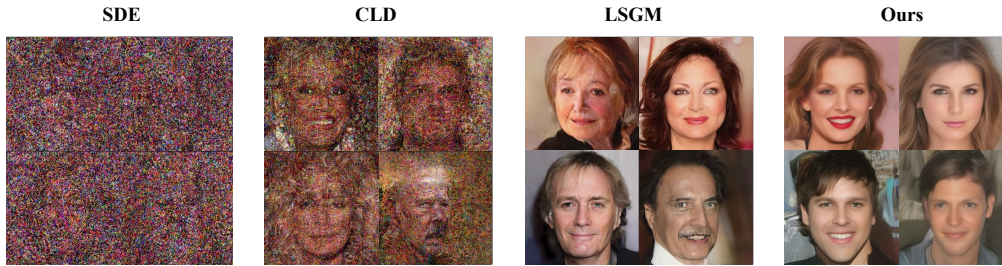


Figure 3: Visual results of unconditional generation with 10 function evaluations on CelebA-HQ-256.

following [29]. We use the AdamW optimizer with scheduled learning rates and train DDM for 800k iterations (the details can be found in supplementary material). We follow [36] using NCSNv2 [34] as the basic model. Differently, since DDM aims to predict the image and noise components separately, we modify the original U-Net architecture by adding an extra decoder. For the conditional generation, we use an additional encoder to extract features for the conditional input and utilize them to relate the features of \mathbf{x}_t by attention mechanisms. For the selection of \mathbf{h}_t , we use a simple yet effective function $\mathbf{h}_t = \mathbf{c}$, and more discussion can be found in Sec. 4.4.

Evaluation. We use Fréchet inception distance (FID) to measure image sample quality for the unconditional image generation task as well as for image inpainting. For super resolution, we use Peak Signal to Noise Ratio (PSNR) to evaluate the image quality. As there is no established metric for the semantic map to image task, we directly compare the visual results. Additionally, we record the number of function evaluations (NFEs) during synthesis when comparing with previous DPMs.

4.2 Unconditional Generation

CIFAR-10. We first present the comparisons between DDM and previous DPMs on the low-resolution dataset CIFAR-10. As shown in Tab. 1, in long-step setting, DDM achieves the FID of 2.19 that outperforms DDPM [13], SDE [36], and CLD [7], and get a comparable performance with LSGM. Note that LSGM uses a much more larger model with 470M parameters while DDM only has 175M. On the other hand, with the benefit of the unique diffusion process, DPM naturally supports few-step generation without ODE-based accelerators. For fair comparison, we uniformly use Euler-Maruyama [2] to solve other diffusion models. From Tab. 1, DDM exceeds all the previous DPMs in few-step setting, especially for 10-step setting we get 13.92 FID outperforming other methods by a large margin. **CelebA-HQ-256.** We conduct experiments on CelebA-HQ-256 to evaluate the generative ability in high-resolution image synthesis. As reported in Tab. 1, we get the best FID of 7.10 for unconditional generation on CelebA-HQ-256. Furthermore, we attain an optimal trade-off between sampling speed and synthesis quality. For example, DPM obtains 27.45 FID just using 10 function evaluations, showcasing its superior efficiency compared to other DPMs. The visual results depicted in Fig. 4 also demonstrate a significant improvement in inpainting quality when utilizing our approach.

Table 2: 10-step conditional generation performances.

	Method	FID↓
Inpainting	DDPM [13]	103.98
	DDM (Ours)	3.65
	Method	PSNR↑
Super Resolution	DDPM [13]	12.46
	DDM (Ours)	27.34

Table 3: Ablation studies of different explicit transition probabilities on CIFAR-10.

$\mathbf{h}_t \setminus \text{NFE}$	10	50	1000
\mathbf{c}	13.92	5.09	2.40
$\mathbf{at} + \mathbf{c}$	15.17	9.69	3.15
$\mathbf{at}^2 + \mathbf{bt} + \mathbf{c}$	22.43	11.05	4.59
$e^{\mathbf{at}} + \mathbf{c}$	28.15	12.15	5.33

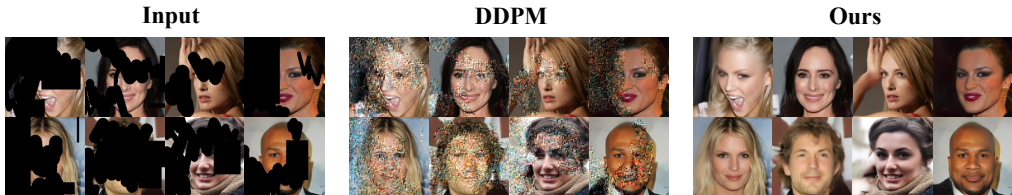


Figure 4: 10-step inpainting visualization.

4.3 Conditional Generation

Image Inpainting. Inpainting is the task of filling masked regions of an image with new content matching the unmasked regions. Using the unmasked image as conditional input, we only evaluate the quality of the inpainted images with 10-step generation for quick comparisons. Tab. 2 reports comparisons of inpainting performances between DDPM [13] and our method. DDM obtains an amazing 3.98 FID, which is more than 30 times lower than that of DDPM, and the visual results show a huge boost as depicted in Fig. 4.

Super Resolution. We use the low-resolution images (128×128) as condition to generate high-resolution images with $4 \times$ larger sizes. Tab. 3 reports the quantitative comparisons of DDPM and our method. Remarkably, we achieve a PSNR of 27.34 using only 10 function evaluations, surpassing DDPM by a significant margin. Furthermore, visual comparisons depicted in Fig. 5 highlight the substantial impact of our approach on the quality of generated images.

Semantic Map to Image. Semantic map to image aims to convert the semantic map containing only the category information of each pixel into a real RGB image. We select the Cityscapes dataset which contains 20 classes of the urban scenes to generate 512×1024 resolution images, which is much challenging. In Fig. 6, we showcase the results of our method and DDPM, with only 10 function evaluations. The generated images exhibit clear contours for different objects, demonstrating the effectiveness of our approach. In comparison, the results obtained by DDPM appear vague.

4.4 Ablation Studies.

We conduct the ablation studies on CIFAR-10 dataset. Eq. 7 shows that we can construct the forward process with arbitrary explicit functions which are obtained by solving $\mathbf{x}_0 + \int_0^1 \mathbf{h}_t dt = \mathbf{0}$. Here, we verify several general functions such as constant function, linear function, quadratic function and exponential function and compare their performances. As shown in Tab. 3, the constant function gets the best performances in all different settings. We think that the constant function only has one learnable term \mathbf{c} , reducing the learning difficulty for the model. On the other hand, the constant

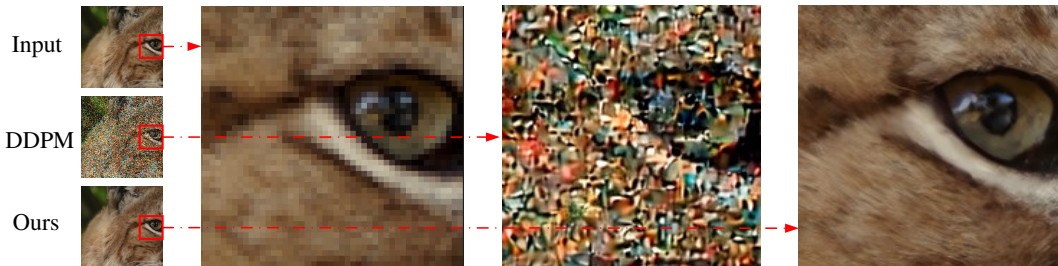


Figure 5: 10-step super-resolution visualization.

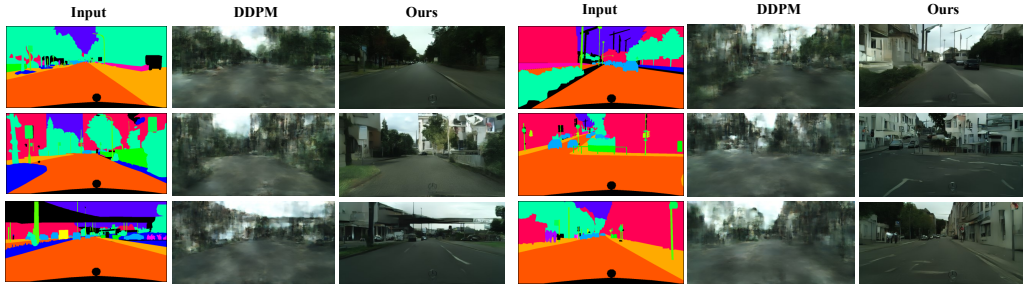


Figure 6: Qualitative results of 10-step generation on semantic map to image task.

function implies that the image component undergoes uniform attenuation during the forward process, providing a clearer and more concise learning pathway.

5 Related Work

Diffusion Probabilistic Models. Diffusion probabilistic models are an emerging generative paradigm that has demonstrated outstanding abilities in several domains, including image generation [6, 14], speech and music synthesis [25], and 3D shape generation [26, 39]. As the proposed DDM provides an alternative framework for common tasks, we primarily focus on discussing the associated diffusion paradigms. Sohl-Dickstein et. al [32] propose the detailed equations of diffusion probabilistic models, and Ho et. al [13] propose a general diffusion framework used in computer vision for the first time. Song et al. [36] establish a link between DPMs and score-based generative models and derived general SDE frameworks for both the forward and reversed processes. Several studies [29, 38] translate the diffusion process from image space to latent space with an auto-encoder, allowing the model to generate higher-resolution images. However, they only translate the data space into a smooth one but not improve the diffusion process itself. CLD [7] introduces the novel velocity variables for the diffusion process to get higher performances and save sampling time, yet it couples the velocity into the image space, resulting in a more complex diffusion process. In contrast, we propose decoupling the previous diffusion process into two relatively simpler processes and introducing an explicit transition probability to model the gradient of the image component.

Few-step Generation with DPMs. Recently, some researchers have focused on accelerating the sampling process for few-step generation. There are two main methods that have been developed to achieve this. One line of work [33, 21, 10, 9, 8] involves constructing ODE solvers of one or higher order to hasten numerical integration in the reversed process. Essentially, they do not change the previous diffusion paradigms, but rather correct the reversed process. Besides, the samples generated from the ODE solvers are determined by the initial noise, which reduces diversity. On the other hand, distillation-based methods [40, 30, 37, 24, 22] suggest using a fitted teacher model to distill the student model, thus allowing the latter to generate with few steps. However, the training process is divided into several stages, which significantly increases the cost of training. Differently, we do not focus on improving the sampling algorithms or training skills, Instead, the proposed DDM is an enhanced diffusion paradigm that naturally supports generating high-quality images with fewer steps.

6 Conclusion

We introduce a new diffusion paradigm called Decoupled Diffusion Models (DDM) that improves the generative abilities of DPMs. In contrast to prior approaches, we propose to simplify the complex diffusion process by decoupling it into two relatively simpler processes, which reduces the learning difficulty caused by the complex SDE. Furthermore, we introduce the explicit transition probability to model the gradient of the image component, resulting in a flexible diffusion process that enables the model to sample with a larger step size. Our experiments demonstrate that DDM outperforms previous DPMs in terms of image synthesis and sampling compute budgets.

Future work and broader impact. In principle, DDM can be combined with high-order ODE solvers to further improve the performance of few-step generation yet we have not derived the formula of high-order solvers. Like other deep generative models, DDM has the potential to transform many

different fields and industries by generating new insights, which makes the long-term social impacts dependent on its downstream applications.

References

- [1] E. Agustsson and R. Timofte. NTIRE 2017 challenge on single image super-resolution: Dataset and study. In *CVPRW*, pages 1122–1131, 2017.
- [2] S. S. Artemiev, S. A. Gusev, and O. G. Monakhov. Numerical solution of stochastic differential equations on transputer network. In J. J. Dongarra, K. Madsen, and J. Wasniewski, editors, *PARA*, pages 33–37, 1995.
- [3] N. Chen, Y. Zhang, H. Zen, R. J. Weiss, M. Norouzi, and W. Chan. Wavegrad: Estimating gradients for waveform generation. In *ICLR*, 2021.
- [4] N. Chen, Y. Zhang, H. Zen, R. J. Weiss, M. Norouzi, N. Dehak, and W. Chan. Wavegrad 2: Iterative refinement for text-to-speech synthesis. In *ISCA*, pages 3765–3769, 2021.
- [5] M. Cordts, M. Omran, S. Ramos, T. Rehfeld, M. Enzweiler, R. Benenson, U. Franke, S. Roth, and B. Schiele. The cityscapes dataset for semantic urban scene understanding. In *CVPR*, 2016.
- [6] P. Dhariwal and A. Nichol. Diffusion models beat gans on image synthesis. In *NeurIPS*, pages 8780–8794, 2021.
- [7] T. Dockhorn, A. Vahdat, and K. Kreis. Score-based generative modeling with critically-damped langevin diffusion. In *ICLR*, 2022.
- [8] T. Dockhorn, A. Vahdat, and K. Kreis. GENIE: higher-order denoising diffusion solvers. In *NeurIPS*, 2022.
- [9] A. Doucet, W. Grathwohl, A. G. de G. Matthews, and H. Strathmann. Score-based diffusion meets annealed importance sampling. In *NeurIPS*, 2022.
- [10] M. K. S. Faradonbeh, M. S. S. Faradonbeh, and M. Bayati. Thompson sampling efficiently learns to control diffusion processes. In *NeurIPS*, 2022.
- [11] I. Goodfellow, J. Pouget-Abadie, M. Mirza, B. Xu, D. Warde-Farley, S. Ozair, A. Courville, and Y. Bengio. Generative adversarial networks. *Communications of the ACM*, 63(11):139–144, 2020.
- [12] J. Ho and T. Salimans. Classifier-free diffusion guidance. *arXiv preprint arXiv:2207.12598*, 2022.
- [13] J. Ho, A. Jain, and P. Abbeel. Denoising diffusion probabilistic models. In *NeurIPS*, pages 6840–6851, 2020.
- [14] J. Ho, C. Saharia, W. Chan, D. J. Fleet, M. Norouzi, and T. Salimans. Cascaded diffusion models for high fidelity image generation. *J. Mach. Learn. Res.*, 23:47:1–47:33, 2022.
- [15] T. Karras, T. Aila, S. Laine, and J. Lehtinen. Progressive growing of gans for improved quality, stability, and variation. In *ICLR*, 2018.
- [16] T. Karras, M. Aittala, T. Aila, and S. Laine. Elucidating the design space of diffusion-based generative models. In *NeurIPS*, 2022.
- [17] D. Kingma, T. Salimans, B. Poole, and J. Ho. Variational diffusion models. In *NeurIPS*, pages 21696–21707, 2021.
- [18] D. P. Kingma and M. Welling. Auto-encoding variational bayes. In *ICLR*, 2014.
- [19] A. Krizhevsky, G. Hinton, et al. Learning multiple layers of features from tiny images. 2009.
- [20] A. W. Lo. Maximum likelihood estimation of generalized itô processes with discretely sampled data. *Econometric Theory*, 4(2):231–247, 1988.

- [21] C. Lu, Y. Zhou, F. Bao, J. Chen, C. Li, and J. Zhu. Dpm-solver: A fast ODE solver for diffusion probabilistic model sampling in around 10 steps. In *NeurIPS*, 2022.
- [22] E. Luhman and T. Luhman. Knowledge distillation in iterative generative models for improved sampling speed. *arXiv preprint arXiv:2101.02388*, 2021.
- [23] S. Luo and W. Hu. Diffusion probabilistic models for 3d point cloud generation. In *CVPR*, pages 2837–2845, 2021.
- [24] C. Meng, R. Gao, D. P. Kingma, S. Ermon, J. Ho, and T. Salimans. On distillation of guided diffusion models. *arXiv preprint arXiv:2210.03142*, 2022.
- [25] G. Mittal, J. H. Engel, C. Hawthorne, and I. Simon. Symbolic music generation with diffusion models. In *ISMIR*, pages 468–475, 2021.
- [26] N. Müller, Y. Siddiqui, L. Porzi, S. R. Bulò, P. Kotschieder, and M. Nießner. Diffrf: Rendering-guided 3d radiance field diffusion. *arXiv preprint arXiv:2212.01206*, 2022.
- [27] A. Q. Nichol and P. Dhariwal. Improved denoising diffusion probabilistic models. In *ICLR*, pages 8162–8171, 2021.
- [28] B. Poole, A. Jain, J. T. Barron, and B. Mildenhall. Dreamfusion: Text-to-3d using 2d diffusion. *arXiv preprint arXiv:2209.14988*, 2022.
- [29] R. Rombach, A. Blattmann, D. Lorenz, P. Esser, and B. Ommer. High-resolution image synthesis with latent diffusion models. In *CVPR*, pages 10674–10685, 2022.
- [30] T. Salimans and J. Ho. Progressive distillation for fast sampling of diffusion models. *arXiv preprint arXiv:2202.00512*, 2022.
- [31] H. Sasaki, C. G. Willcocks, and T. P. Breckon. Unit-ddpm: Unpaired image translation with denoising diffusion probabilistic models. *arXiv preprint arXiv:2104.05358*, 2021.
- [32] J. Sohl-Dickstein, E. Weiss, N. Maheswaranathan, and S. Ganguli. Deep unsupervised learning using nonequilibrium thermodynamics. In *ICLR*, pages 2256–2265, 2015.
- [33] J. Song, C. Meng, and S. Ermon. Denoising diffusion implicit models. In *ICLR*, 2021.
- [34] Y. Song and S. Ermon. Improved techniques for training score-based generative models. pages 12438–12448, 2020.
- [35] Y. Song, C. Durkan, I. Murray, and S. Ermon. Maximum likelihood training of score-based diffusion models. In *NeurIPS*, pages 1415–1428, 2021.
- [36] Y. Song, J. Sohl-Dickstein, D. P. Kingma, A. Kumar, S. Ermon, and B. Poole. Score-based generative modeling through stochastic differential equations. In *ICLR*, 2021.
- [37] Y. Song, P. Dhariwal, M. Chen, and I. Sutskever. Consistency models. *arXiv preprint arXiv:2303.01469*, 2023.
- [38] A. Vahdat, K. Kreis, and J. Kautz. Score-based generative modeling in latent space. In M. Ranzato, A. Beygelzimer, Y. N. Dauphin, P. Liang, and J. W. Vaughan, editors, *NeurIPS*, pages 11287–11302, 2021.
- [39] T. Wang, B. Zhang, T. Zhang, S. Gu, J. Bao, T. Baltrusaitis, J. Shen, D. Chen, F. Wen, Q. Chen, et al. Rodin: A generative model for sculpting 3d digital avatars using diffusion. *arXiv preprint arXiv:2212.06135*, 2022.
- [40] Q. Zhang and Y. Chen. Fast sampling of diffusion models with exponential integrator. *arXiv preprint arXiv:2204.13902*, 2022.

Supplementary Material of Decoupled Diffusion Models with Explicit Transition Probability

Anonymous Author(s)

Affiliation

Address

email

1 Proofs and Derivations

2 1.1 Equivalence between DDM and previous diffusion process [?]

3 The previous study [?] has proved that the mapping from the image to noise can be formulated by a
4 Stochastic Differential Equation (SDE):

$$d\mathbf{x}_t = f_t \mathbf{x}_t dt + g_t d\mathbf{w}_t, \quad \mathbf{x}_0 \sim q(\mathbf{x}_0), \quad (1)$$

5 where $f_t \mathbf{x}_t$ and g_t represent the drift term and diffusion term of the Itô diffusion process [?]. Our
6 decoupled diffusion process is directly described by the Itô integral that can be formulated by:

$$\mathbf{x}_t = \mathbf{x}_0 + \int_0^t \mathbf{h}_t dt + \int_0^t d\mathbf{w}_t, \quad \mathbf{x}_0 \sim q(\mathbf{x}_0). \quad (2)$$

7 Taking the derivative of the above formula, we get the similar differential form to Eq. 1:

$$d\mathbf{x}_t = \mathbf{h}_t dt + d\mathbf{w}_t, \quad \mathbf{h}_t \sim \int_0^t \mathbf{h}_t dt + \mathbf{x}_0 = \mathbf{0}, \quad \mathbf{x}_0 \sim q(\mathbf{x}_0), \quad (3)$$

8 Comparing Eq. 1 and Eq. 3, we can prove that the two formulas are equal when $f_t \mathbf{x}_t = h_t$ and $g_t = 1$.
9 Therefore, the proposed decoupled diffusion process is equivalent to previous diffusion processes
10 described by Eq. 1. Actually, our decoupled diffusion formula is a special form of Eq. 1 that they
11 both can describe the mapping from the image to noise. Differently, the decoupled process allows the
12 model to learn the image and noise components independently. We split the complex mapping from
13 the original image to noise into two relatively simpler processes, reducing the learning difficulty and
14 enabling using a explicit transition probability to model the image component.

15 **1.2 Proof of Training Objective**

16 We can derive the training objective of DDM by maximizing the evidence lower bound of the
 17 log-likelihood $\log p(\mathbf{x})$. Considering the continuous-time Markov chain, $\log p(\mathbf{x})$ is represented by:

$$\begin{aligned}
 \log p(\mathbf{x}) &= \log \int p(\mathbf{x}_{0:1}) d\mathbf{x}_{\Delta t:1}, \Delta t \rightarrow 0^+ \\
 &= \log \int \frac{p(\mathbf{x}_{0:1})q(\mathbf{x}_{\Delta t:1}|\mathbf{x}_0)}{q(\mathbf{x}_{\Delta t:1}|\mathbf{x}_0)} d\mathbf{x}_{\Delta t:1} \\
 &= \log \mathbb{E}_q \left[\frac{p(\mathbf{x}_{0:1})}{q(\mathbf{x}_{\Delta t:1}|\mathbf{x}_0)} \right] \\
 &\geq \mathbb{E}_q \left[\log \frac{p(\mathbf{x}_{0:1})}{q(\mathbf{x}_{\Delta t:1}|\mathbf{x}_0)} \right] \quad \# \text{Jensen's inequality} \\
 &= \mathbb{E}_q \left[\log \frac{p(\mathbf{x}_1) \prod_{t=\Delta t}^1 p_{\theta}(\mathbf{x}_{t-\Delta t}|\mathbf{x}_t)}{\prod_{t=\Delta t}^1 q(\mathbf{x}_t|\mathbf{x}_{t-\Delta t})} \right] \\
 &= \mathbb{E}_q \left[\log \frac{p(\mathbf{x}_1) \prod_{t=\Delta t}^1 p_{\theta}(\mathbf{x}_{t-\Delta t}|\mathbf{x}_t)}{\prod_{t=\Delta t}^1 q(\mathbf{x}_t|\mathbf{x}_{t-\Delta t}, \mathbf{x}_0)} \right] \quad \# \text{Markov property} \\
 &= \mathbb{E}_q \left[\log \frac{p(\mathbf{x}_1) \prod_{t=\Delta t}^1 p_{\theta}(\mathbf{x}_{t-\Delta t}|\mathbf{x}_t) q(\mathbf{x}_{t-\Delta t}|\mathbf{x}_0)}{\prod_{t=\Delta t}^1 q(\mathbf{x}_{t-\Delta t}|\mathbf{x}_t, \mathbf{x}_0) q(\mathbf{x}_t|\mathbf{x}_0)} \right] \quad \# \text{Bayes rule} \\
 &= \mathbb{E}_q \left[\log \frac{p(\mathbf{x}_1) \prod_{t=\Delta t}^1 p_{\theta}(\mathbf{x}_{t-\Delta t}|\mathbf{x}_t)}{\prod_{t=\Delta t}^1 q(\mathbf{x}_{t-\Delta t}|\mathbf{x}_t, \mathbf{x}_0)} + \log \frac{\prod_{t=\Delta t}^1 q(\mathbf{x}_{t-\Delta t}|\mathbf{x}_0)}{\prod_{t=\Delta t}^1 q(\mathbf{x}_t|\mathbf{x}_0)} \right] \\
 &= \mathbb{E}_q \left[\log \frac{p(\mathbf{x}_1) \prod_{t=\Delta t}^1 p_{\theta}(\mathbf{x}_{t-\Delta t}|\mathbf{x}_t)}{\prod_{t=\Delta t}^1 q(\mathbf{x}_{t-\Delta t}|\mathbf{x}_t, \mathbf{x}_0)} + \log \frac{1}{q(\mathbf{x}_1|\mathbf{x}_0)} \right] \\
 &= \mathbb{E}_q \left[\log \frac{p(\mathbf{x}_1)}{q(\mathbf{x}_1|\mathbf{x}_0)} + \log \frac{\prod_{t=\Delta t}^1 p_{\theta}(\mathbf{x}_{t-\Delta t}|\mathbf{x}_t)}{\prod_{t=\Delta t}^1 q(\mathbf{x}_{t-\Delta t}|\mathbf{x}_t, \mathbf{x}_0)} \right] \\
 &= \mathbb{E}_q \left[\log \frac{p(\mathbf{x}_1)}{q(\mathbf{x}_1|\mathbf{x}_0)} \right] - \prod_{t=\Delta t}^1 \mathbb{E}_q [D_{KL}(q(\mathbf{x}_{t-\Delta t}|\mathbf{x}_t, \mathbf{x}_0) || p_{\theta}(\mathbf{x}_{t-\Delta t}|\mathbf{x}_t))]
 \end{aligned} \tag{4}$$

18 The first term in the equation can be interpreted as the prior matching term, which ensures that the
 19 original data can be transformed into the noise distribution when $t = 1$. It has been demonstrated
 20 in Section 3 of the main paper that our forward process satisfies this requirement, eliminating the
 21 need to construct a loss function for this term. On the other hand, the latter term represents the
 22 denoising matching term and its purpose is to ensure consistency in the distribution at \mathbf{x}_t from both
 23 the forward and reversed processes. To achieve this, we aim to learn the desired denoising tran-
 24 sition step $p_{\theta}(\mathbf{x}_{t-\Delta t}|\mathbf{x}_t)$ as an approximation to the tractable ground-truth denoising transition step
 25 $q(\mathbf{x}_{t-\Delta t}|\mathbf{x}_t, \mathbf{x}_0)$. Minimizing this term entails achieving the closest possible match between the two
 26 denoising steps, as quantified by their KL Divergence. In fact, the ground-truth denoising tran-
 27 sition step $q(\mathbf{x}_{t-\Delta t}|\mathbf{x}_t, \mathbf{x}_0)$ is still a normal distribution. Therefore, minimizing the KL Divergence is
 28 equivalent to minimizing the error between their mean and variance, which means we can use the
 29 MSE (mean squared error) function to formulate the training object.

30 We first prove the normality of $q(\mathbf{x}_{t-\Delta t}|\mathbf{x}_t, \mathbf{x}_0)$. Giving the forward transition probability $q(\mathbf{x}_t|\mathbf{x}_0) =$
 31 $\mathcal{N}(\mathbf{x}_t; \mathbf{x}_0 + \mathbf{H}_t, t\mathbf{I})$, we have:

$$\begin{aligned}
 q(\mathbf{x}_{t-\Delta t}|\mathbf{x}_t, \mathbf{x}_0) &= \frac{q(\mathbf{x}_t|\mathbf{x}_{t-\Delta t}, \mathbf{x}_0)q(\mathbf{x}_{t-\Delta t}|\mathbf{x}_0)}{q(\mathbf{x}_t|\mathbf{x}_0)} \\
 &= \frac{q(\mathbf{x}_t|\mathbf{x}_{t-\Delta t})q(\mathbf{x}_{t-\Delta t}|\mathbf{x}_0)}{q(\mathbf{x}_t|\mathbf{x}_0)} \quad \# \text{Markov property} \\
 &= \frac{q(\mathbf{x}_t|\mathbf{x}_{t-\Delta t})\mathcal{N}(\mathbf{x}_{t-\Delta t}; \mathbf{x}_0 + \mathbf{H}_{t-\Delta t}, (t - \Delta t)\mathbf{I})}{\mathcal{N}(\mathbf{x}_t; \mathbf{x}_0 + \mathbf{H}_t, t\mathbf{I})}.
 \end{aligned} \tag{5}$$

32 Here, we can easily prove that $q(\mathbf{x}_t|\mathbf{x}_{t-\Delta t})$ is also a normal distribution by the following derivation:

$$\begin{aligned}
\mathbf{x}_t &= \mathbf{x}_0 + \mathbf{H}_t + \sqrt{t}\boldsymbol{\epsilon}, \boldsymbol{\epsilon} \sim \mathcal{N}(\mathbf{0}, \mathbf{I}) \\
&= \mathbf{x}_0 + \mathbf{H}_t - \mathbf{H}_{t-\Delta t} + \mathbf{H}_{t-\Delta t} + \sqrt{t-\Delta t}\boldsymbol{\epsilon}_1 + \sqrt{\Delta t}\boldsymbol{\epsilon}_2, \boldsymbol{\epsilon}_1, \boldsymbol{\epsilon}_2 \sim \mathcal{N}(\mathbf{0}, \mathbf{I}) \\
&= \mathbf{x}_0 + \mathbf{H}_{t-\Delta t} + \sqrt{t-\Delta t}\boldsymbol{\epsilon}_1 + \mathbf{H}_t - \mathbf{H}_{t-\Delta t} + \sqrt{\Delta t}\boldsymbol{\epsilon}_2 \\
&= \mathbf{x}_{t-\Delta t} + \mathbf{H}_t - \mathbf{H}_{t-\Delta t} + \sqrt{\Delta t}\boldsymbol{\epsilon}_2. \quad \# \text{Definition of } q(\mathbf{x}_t|\mathbf{x}_0)
\end{aligned} \tag{6}$$

33 Thus, $q(\mathbf{x}_t|\mathbf{x}_{t-\Delta t})$ is the normal distribution with mean $\mathbf{x}_{t-\Delta t} + \mathbf{H}_t - \mathbf{H}_{t-\Delta t}$ and variance $\Delta t\mathbf{I}$:

$$q(\mathbf{x}_t|\mathbf{x}_{t-\Delta t}) = \mathcal{N}(\mathbf{x}_t; \mathbf{x}_{t-\Delta t} + \mathbf{H}_t - \mathbf{H}_{t-\Delta t}, \Delta t\mathbf{I}). \tag{7}$$

34 Substituting Eq. 7 into Eq. 5, we have:

$$\begin{aligned}
q(\mathbf{x}_{t-\Delta t}|\mathbf{x}_t, \mathbf{x}_0) &= \frac{q(\mathbf{x}_t|\mathbf{x}_{t-\Delta t})\mathcal{N}(\mathbf{x}_{t-\Delta t}; \mathbf{x}_0 + \mathbf{H}_{t-\Delta t}, (t-\Delta t)\mathbf{I})}{\mathcal{N}(\mathbf{x}_t; \mathbf{x}_0 + \mathbf{H}_t, t\mathbf{I})} \\
&\propto \exp\left\{-\frac{1}{2}\left[\frac{(\mathbf{x}_t - \mathbf{x}_{t-\Delta t} - \mathbf{H}_t + \mathbf{H}_{t-\Delta t})^2}{\Delta t} + \frac{(\mathbf{x}_{t-\Delta t} - \mathbf{x}_0 - \mathbf{H}_{t-\Delta t})^2}{t-\Delta t}\right]\right\} \\
&= \exp\left\{-\frac{1}{2}\left[\frac{t}{\Delta t(t-\Delta t)}\mathbf{x}_{t-\Delta t}^2\right.\right. \\
&\quad \left.\left.+ \frac{\Delta t\mathbf{x}_0 + (t-\Delta t)(\mathbf{x}_t - \mathbf{H}_t) + t\mathbf{H}_{t-\Delta t}}{\Delta t(t-\Delta t)}(2\mathbf{x}_{t-\Delta t}) + C\right]\right\},
\end{aligned} \tag{8}$$

35 where C is the term not related to $\mathbf{x}_{t-\Delta t}$. Eq. 8 contains \mathbf{x}_0 which is known in the forward process,
36 and we can directly get the prior \mathbf{x}_0 from the forward transition probability $q(\mathbf{x}_t|\mathbf{x}_0)$:

$$\mathbf{x}_0 = \mathbf{x}_t - \mathbf{H}_t - \sqrt{t}\boldsymbol{\epsilon}. \tag{9}$$

37 Comparing Eq. 8 with the standard normal distribution and substituting Eq. 9 into Eq. 8, we can
38 obtain the mean $\tilde{\mathbf{u}}$ and variance $\tilde{\sigma}^2$ of $q(\mathbf{x}_{t-\Delta t}|\mathbf{x}_t, \mathbf{x}_0)$:

$$\begin{aligned}
\tilde{\mathbf{u}} &= \mathbf{x}_t + \mathbf{H}_{t-\Delta t} - \mathbf{H}_t - \frac{\Delta t}{\sqrt{t}}\boldsymbol{\epsilon}, \\
\tilde{\sigma}^2 &= \frac{\Delta t(t-\Delta t)}{t}.
\end{aligned} \tag{10}$$

39 Thus, the proof of $q(\mathbf{x}_{t-\Delta t}|\mathbf{x}_t, \mathbf{x}_0)$ is complete.

40 We use a neural network with parameters $\boldsymbol{\theta}$ to parameterize $p_{\boldsymbol{\theta}}(\mathbf{x}_{t-\Delta t}|\mathbf{x}_t)$. In practice, the variance
41 $\tilde{\sigma}^2$ only depends on t and Δt so we only need to parameterize the mean. From Eq. 4, we can optimize
42 $\boldsymbol{\theta}$ by minimizing the KL Divergence:

$$\begin{aligned}
&\min_{\boldsymbol{\theta}} D_{KL}(q(\mathbf{x}_{t-\Delta t}|\mathbf{x}_t, \mathbf{x}_0)||p_{\boldsymbol{\theta}}(\mathbf{x}_{t-\Delta t}|\mathbf{x}_t)) \\
&= \min_{\boldsymbol{\theta}} D_{KL}(\mathcal{N}(\mathbf{x}_{t-\Delta t}; \tilde{\mathbf{u}}, \tilde{\sigma}^2\mathbf{I})||\mathcal{N}(\mathbf{x}_{t-\Delta t}; \mathbf{u}_{\boldsymbol{\theta}}, \tilde{\sigma}^2\mathbf{I})) \\
&= \min_{\boldsymbol{\theta}} \frac{1}{2}(\mathbf{u}_{\boldsymbol{\theta}} - \tilde{\mathbf{u}})^T(\tilde{\sigma}^2\mathbf{I})^{-1}(\mathbf{u}_{\boldsymbol{\theta}} - \tilde{\mathbf{u}}) \\
&= \min_{\boldsymbol{\theta}} \frac{1}{2\tilde{\sigma}^2}\|\mathbf{u}_{\boldsymbol{\theta}} - \tilde{\mathbf{u}}\|^2.
\end{aligned} \tag{11}$$

43 As $\mathbf{u}_{\boldsymbol{\theta}}$ is also conditioned on \mathbf{x}_t , we can match $\tilde{\mathbf{u}}$ closely by setting it to the following form:

$$\mathbf{u}_{\boldsymbol{\theta}} = \mathbf{x}_t + \mathbf{H}_{\boldsymbol{\theta}t-\Delta t} - \mathbf{H}_{\boldsymbol{\theta}t} - \frac{\Delta t}{\sqrt{t}}\boldsymbol{\epsilon}_{\boldsymbol{\theta}}. \tag{12}$$

44 Then, the optimization problem simplifies to:

$$\begin{aligned}
& \min_{\theta} D_{KL}(q(\mathbf{x}_{t-\Delta t}|\mathbf{x}_t, \mathbf{x}_0)||p_{\theta}(\mathbf{x}_{t-\Delta t}|\mathbf{x}_t)) \\
&= \min_{\theta} \frac{1}{2\tilde{\sigma}^2} \left\| (\mathbf{x}_t + \mathbf{H}_{\theta_{t-\Delta t}} - \mathbf{H}_{\theta_t} - \frac{\Delta t}{\sqrt{t}}\epsilon_{\theta}) - (\mathbf{x}_t + \mathbf{H}_{t-\Delta t} - \mathbf{H}_t - \frac{\Delta t}{\sqrt{t}}\epsilon) \right\|^2 \\
&= \min_{\theta} \frac{1}{2\tilde{\sigma}^2} \left\| \int_t^{t-\Delta t} \mathbf{h}_{\theta_t} dt - \int_t^{t-\Delta t} \mathbf{h}_t dt + \frac{\Delta t}{\sqrt{t}}(\epsilon_{\theta} - \epsilon) \right\|^2 \\
&= \min_{\theta} \frac{1}{2\tilde{\sigma}^2} \left\| \int_t^{t-\Delta t} \mathbf{h}_{\theta_t} - \mathbf{h}_t dt + \frac{\Delta t}{\sqrt{t}}(\epsilon_{\theta} - \epsilon) \right\|^2 \\
&= : \min_{\theta} \frac{1}{2\tilde{\sigma}^2} \|\mathbf{h}_{\theta_t} - \mathbf{h}_t\|^2 + \frac{1}{2\tilde{\sigma}^2} \left\| \frac{\Delta t}{\sqrt{t}}(\epsilon_{\theta} - \epsilon) \right\|^2 \\
&= \min_{\theta} \frac{1}{2\tilde{\sigma}^2} \|\mathbf{h}_{\theta_t} - \mathbf{h}_t\|^2 + \frac{\Delta t^2}{2\tilde{\sigma}^2 t} \|\epsilon_{\theta} - \epsilon\|^2.
\end{aligned} \tag{13}$$

45 As \mathbf{h}_t depends on \mathbf{h}_t and \mathbf{h}_t is determined by its hyper-parameters ϕ that can be solved using
46 $\mathbf{x}_0 + \int_0^1 \mathbf{h}_t dt = \mathbf{0}$, we can directly parameterize ϕ using ϕ_{θ} . Thus, the training objective is
47 formulated by:

$$\begin{aligned}
& \min_{\theta} D_{KL}(q(\mathbf{x}_{t-\Delta t}|\mathbf{x}_t, \mathbf{x}_0)||p_{\theta}(\mathbf{x}_{t-\Delta t}|\mathbf{x}_t)) \\
&= \min_{\theta} \frac{1}{2\tilde{\sigma}^2} \|\phi_{\theta} - \phi\|^2 + \frac{\Delta t^2}{2\tilde{\sigma}^2 t} \|\epsilon_{\theta} - \epsilon\|^2.
\end{aligned} \tag{14}$$

48 The proof of our training objective is completed. In essential, ϕ represents the original image
49 component while ϵ can be seen as the noise distribution. Therefore, the training objective allows the
50 model to learn the image and the noise components independently.

51 1.3 Derivation of Few-step Sampling Formula

52 Different from previous diffusion probabilistic models (DPMs), the proposed DDM naturally enables
53 few-step sampling. Following Eq.6, we have:

$$\begin{aligned}
\mathbf{x}_t &= \mathbf{x}_0 + \mathbf{H}_t + \sqrt{t}\epsilon, \epsilon \sim \mathcal{N}(\mathbf{0}, \mathbf{I}) \\
&= \mathbf{x}_0 + \mathbf{H}_t - \mathbf{H}_{t-s} + \mathbf{H}_{t-s} + \sqrt{t-s}\epsilon_1 + \sqrt{s}\epsilon_2, \epsilon_1, \epsilon_2 \sim \mathcal{N}(\mathbf{0}, \mathbf{I}) \\
&= \mathbf{x}_0 + \mathbf{H}_{t-s} + \sqrt{t-s}\epsilon_1 + \mathbf{H}_t - \mathbf{H}_{t-s} + \sqrt{s}\epsilon_2 \\
&= \mathbf{x}_{t-s} + \mathbf{H}_t - \mathbf{H}_{t-s} + \sqrt{s}\epsilon_2. \quad \# \text{Definition of } q(\mathbf{x}_t|\mathbf{x}_0)
\end{aligned} \tag{15}$$

54 Thus, we can give the transition probability $q(\mathbf{x}_t|\mathbf{x}_{t-s})$ for an arbitrary step size s :

$$q(\mathbf{x}_t|\mathbf{x}_{t-s}) = \mathcal{N}(\mathbf{x}_t; \mathbf{x}_{t-s} + \mathbf{H}_t - \mathbf{H}_{t-s}, s\mathbf{I}). \tag{16}$$

55 With Eq. 16, we can easily derive the mean and variance of $q(\mathbf{x}_{t-s}|\mathbf{x}_t, \mathbf{x}_0)$ following Eq. 8:

$$\begin{aligned}
q(\mathbf{x}_{t-s}|\mathbf{x}_t, \mathbf{x}_0) &\propto \exp\left\{-\frac{(\mathbf{x}_{t-s} - \tilde{\mathbf{u}})^2}{2\tilde{\sigma}^2\mathbf{I}}\right\}, \\
\tilde{\mathbf{u}} &= \mathbf{x}_t + \mathbf{H}_{t-s} - \mathbf{H}_t - \frac{s}{\sqrt{t}}\epsilon, \\
\tilde{\sigma}^2 &= \frac{s(t-s)}{t}.
\end{aligned} \tag{17}$$

56 Eq. 17 means DDM can sample with any step sizes even using the largest step size $s = 1$ for one-step
57 generation. However, it is challenging to estimate an exactly accurate ϕ at the initial time, and
58 one-step generation causes the variance $\tilde{\sigma}^2$ to be zero. This results in the generated images appearing
59 somewhat blurry and lacking diversity. Therefore, we still sample iteratively but use a much larger
60 step size than previous DPMs, reducing the sampling steps from 1000 to 10 drastically. We commence
61 at $t = 1$ and take uniform steps of size s until we reach $t = 0$.

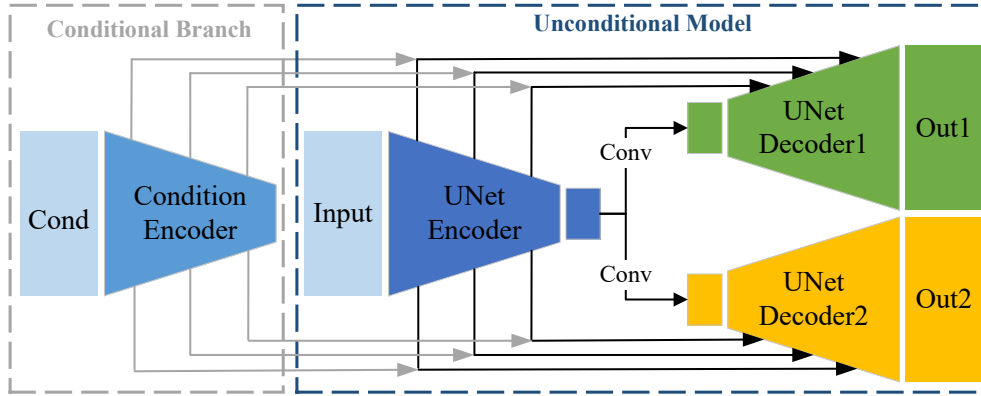


Figure 1: Architecture detail. The ‘Cond’ represents the conditional input and the conditional branch is only used in conditional generation tasks.

62 2 More Details of Experiments

63 2.1 Architecture of Network

64 As shown in Fig. 1, we modify the original UNet architecture [?] and add an extra decoder so that
 65 our model has two outputs for predicting image and noise components respectively. For conditional
 66 generation tasks, we utilize a down-sampling encoder like the UNet encoder to extract multi-level
 67 features of the conditional input, and concatenate these features and the image features with the same
 68 levels as the decoder’s inputs.

69 2.2 Training Details

70 **Hyper-parameters.** We provide an overview of the hyper-parameters of all trained DDMs in
 71 Tab. 1. Different from previous models that usually adopt a constant learning rate, we implement
 72 the polynomial policy to decay the learning rate gradually, which can be formulated by: $\gamma =$
 73 $\max(\gamma_0 \cdot (1 - N_{iter}/N_{total})^p, \gamma_{min})$. Here γ_0 is the initial learning rate and γ_{min} denotes the
 74 smallest learning rate, N_{iter} and N_{total} correspond to the current iteration number and total iteration
 75 number, p a hyper-parameter and we set it to 0.96. Additionally, we employ the exponential moving
 76 average (EMA) to prevent unstable model performances during the training process. We have
 77 observed that using mixed-precision (FP16) training negatively impacts the generative performances,
 78 hence, we do not utilize it.

79 **Additional Implementation Details.** We find the closer t is to 0, the more accurate the prediction
 80 ϕ will be, and it is opposite for predicting ϵ . To alleviate this problem, we empirically set a scale
 81 factor $\exp(t)$ for predicting ϕ and another scale factor $\sqrt{\exp(1-t)}$ for ϵ . For the inpainting and
 82 semantic map to image tasks, we add the learnable positional encodings to the masks, increasing the
 83 expression ability of the binary features. We use both L1 and L2 losses to supervise the network in
 84 the training stage.

85 **Final Denoising Step.** In general, the generated samples typically contain small noise that is hard to
 86 detect by humans [?]. To remove this noise, we follow [?] letting the last denoising step occur at
 87 $t = \Delta t$ where Δt is the smallest step size.

88 2.3 Additional Visual Results

89 We present more visual comparisons in the following figures: Fig. 2 shows the visual comparisons
 90 between DDM and other DPMs on CIFAR10 dataset, and Fig. 3 shows the visual comparisons
 91 on CelebA-HQ-256 dataset. Additionally, we show more visual results of both unconditional and
 92 conditional generation tasks in Fig. 4- 7, which demonstrates our method can generate high-quality
 93 images only using 10 function evaluations.

Table 1: Hyper-parameters for the trained DDMs.

Task	Unconditional generation		Inpainting	Super Resolution	Semantic map to image
	CIFAR10	CelebA-HQ-256			
Image size	32×32	256×256	256×256	512×512	512×1024
Batch size	128	48	48	12	4
Learning rate	1e-4~1e-5	6e-5~6e-6	4e-5~4e-6	5e-5~5e-6	1e-5~5e-6
Iterations	800k	800k	400k	400k	400k
Feature channels	128	128	96	128	128
Channel multiplier	[1,2,2,2]	[1,2,2,2]	[1,2,4,8]	[1, 2, 4, 4, 4]	[1, 2, 4, 4, 4]
Number of blocks	8	8	2	2	2
Smallest time step	1e-4	1e-4	1e-4	2e-4	2e-4

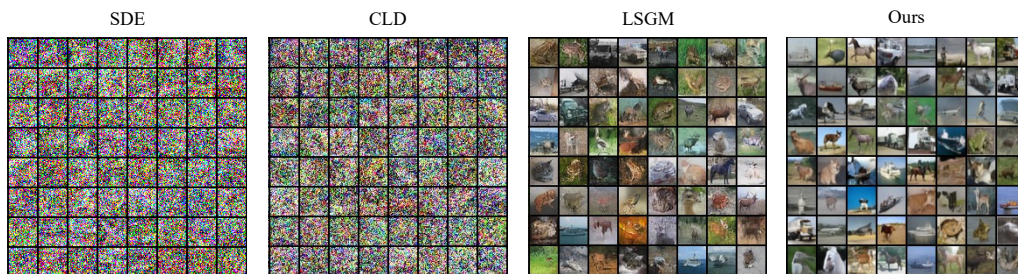


Figure 2: Comparisons of 10-step unconditional generation on CIFAR10.

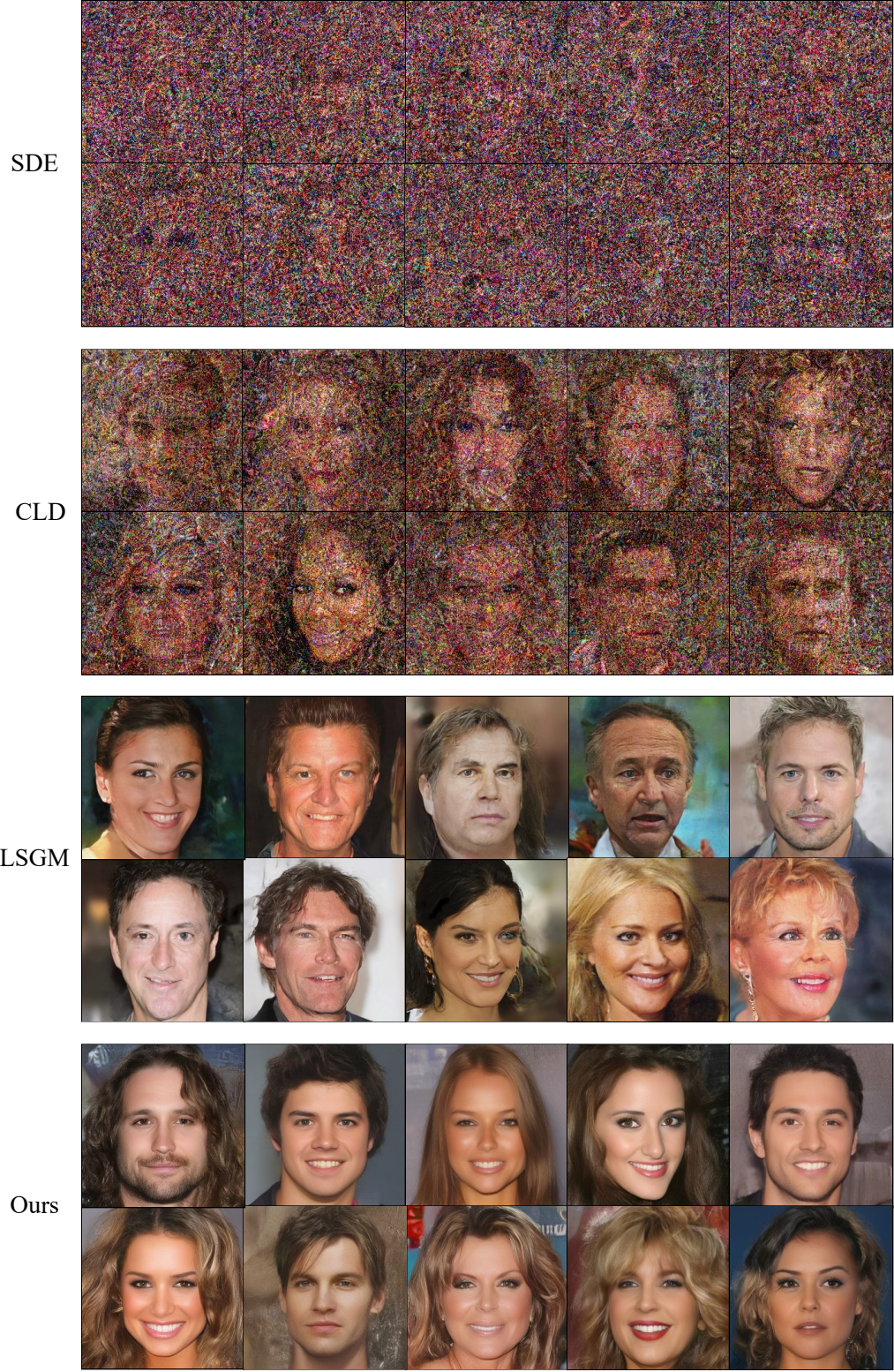


Figure 3: Comparisons of 10-step unconditional generation on CelebA-HQ-256.



Figure 4: 10-step unconditional generation on CIFAR-10.



Figure 5: 10-step unconditional generation on CelebA-HQ-256.

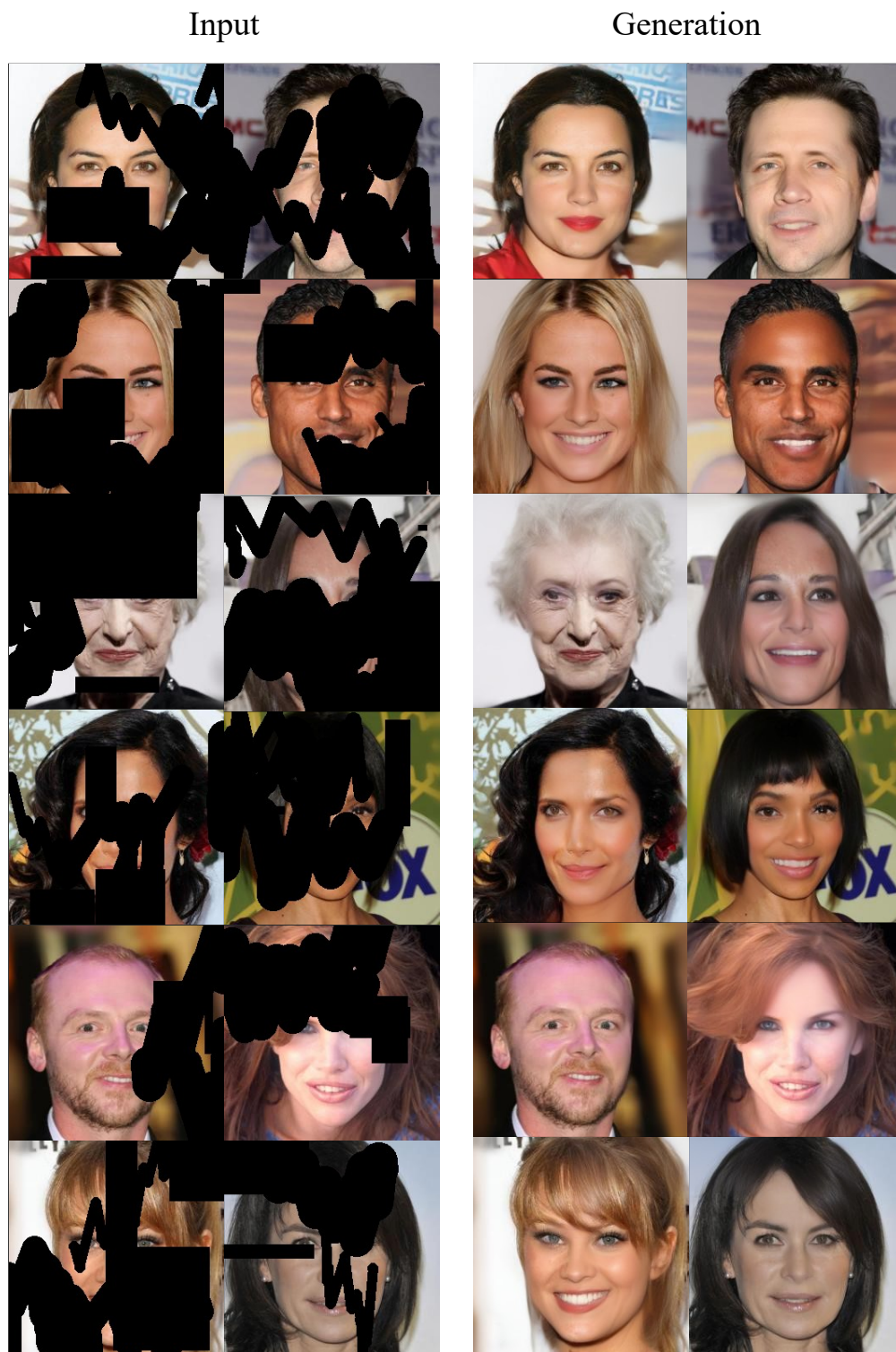


Figure 6: 10-step inpainting visualization.

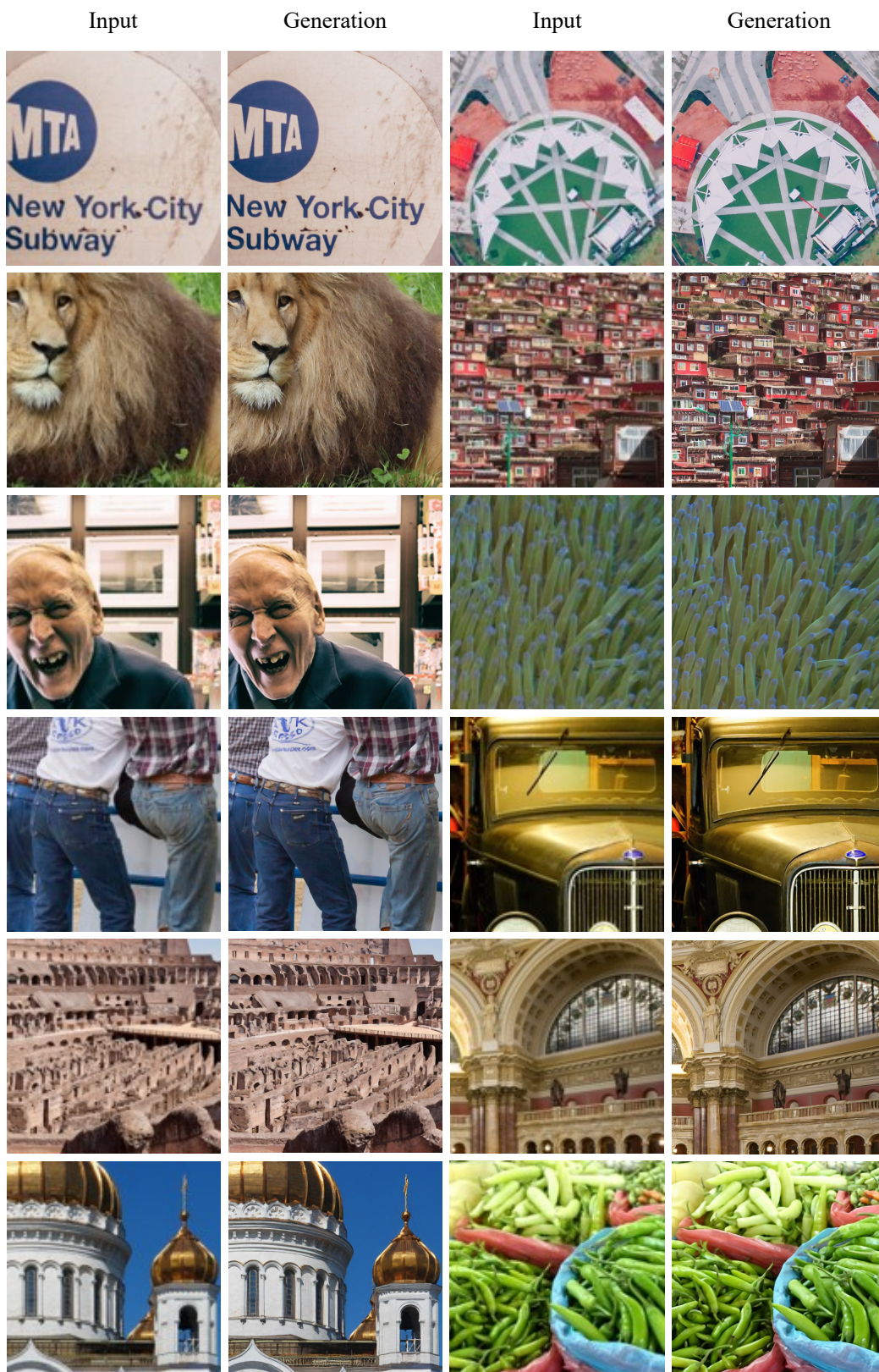


Figure 7: 10-step super-resolution visualization.